Geomechanics and Engineering, *Vol. 40, No. 1 (2025) 1-11*
https://doi.org/10.12989/gae.2025.40.1.001

Assessing influence of waves on riverbank stability: A centrifuge modeling approach

Canh M. Tran*[1], Yi W. Hung[2a], Farid Sitepu[2b], Giang H.H. Pham[3c] and Em L. Huynh[4d]

[1]*Earth Sciences and Geotechnical Engineering Division, National Center for Earthquake Engineering, R.O.C Taiwan*
[2]*Department of Civil Engineering, National Central University, R.O.C, Taiwan*
[3]*Faculty of Transportation Engineering, Can Tho University, VietNam*
[4]*Faculty of Civil Engineering, Industrial University of Ho Chi Minh City, VietNam*

(*Received April 23, 2024, Revised December 23, 2024, Accepted December 24, 2024*)

Abstract. Erosion along riverbanks stands as a critical natural disaster, severely impacting the economy and livelihoods of those near rivers. The erosion occurs from the weakening and displacement of materials along the bank, driven by various elements such as water flow, ship-generated waves, agricultural practices, and nearby infrastructure. The soil-water interface presents a complex challenge, sparking extensive studies into understanding the interplay between hydrodynamic forces and soil properties. This research focuses on assessing how water waves influence riverbank stability. Through a series of centrifuge experiments, it investigates the relationship between wave-induced dynamic pressure and erosion rates. Findings suggest that the wave height of 0.22 to 0.24 meters on the prototype scale can be simulated under a 20 g artificial acceleration in the centrifuge modelling. The erosion process develops in three distinct phases: initial erosion, formation of tension cracks, and eventual collapse, underscoring the practical importance of understanding wave pressure and soil resistance to predict erosion rates and design effective mitigation measures for riverbank and geotechnical structures.

Keywords: centrifuge modeling; erosion rate; impact pressure; riverbank; soil-water interaction;waves

1. Introduction

Riverbank erosion stands out as a natural disaster, exerting substantial adverse impacts on the economies and livelihoods of communities residing along riverbanks. This phenomenon arises from the erosion of riverbank materials, facilitated by elements such as water currents, ship-generated waves, agricultural activities, and riverbank infrastructures. These factors contribute to relocating materials to sediment areas, altering the slope geometry, and compromising the original stability. Numerous regions grapple with the consequences of this disaster, affecting millions of people, causing extensive damage to agricultural lands spanning thousands of kilometers, and resulting in significant population displacement. Research into the processes of riverbank erosion and associated landforms has been conducted across diverse geographical and hydrological conditions.

In July 2020, there was a riverbank erosion event along the Hau River in An Giang Province, VietNam, spanning 300 meters and impacting 44 households in the Mekong Delta. A similar incident occurred in 2019, destroying a 100-meter asphalt road, with repairs costing over 250 billion VND (Nguyen *et al*. 2021, Van *et al*. 2021).

The Yangtze River, the world's third-longest at around 6,300 kilometers, experiences severe soil erosion, losing approximately 2.24 billion tons of soil each year. This erosion affects nearly 67,000 hectares of agricultural land and poses threats to the livelihoods and safety of about 400 million people living along its basin (Zheng *et al.* 2018, Yan *et al.* 2022, Zhou *et al*. 2024). In Bangladesh, about 5% of floodplains are impacted by erosion, resulting in an annual loss of around 2,600 hectares of land. Over a 28-year period, the total loss has reached around 70,000 hectares. Some riverbanks retreat by as much as 66 meters per year, with extreme cases reaching 184 meters per year. These conditions lead to crop failures, displacement of households, and significant economic and social hardship (Paul *et al*. 2020, Mondal *et al.* 2021, Oberhagemann *et al.* 2011, Billah *et al.* 2023).

Despite being more commonly associated with tropical areas, riverbank erosion also occurs in cold environments (Prowse *et al.* 2003, Vandermause *et al.* 2021). Cold areas, such as the Susitna River in Alaska, experience riverbank erosion due to gouging and abrasion during ice-break-up events (Beltaos *et al.* 2018, Chassiot *et al.* 2020). The erosion process in cold areas is more intricate, prompting scientific studies to predict and mitigate its impacts.

The investigation into the impact of fluvial hydraulic forces on riverbank processes has involved a variety of research methods, including physical modeling and numerical modeling, as evidenced in studies by Kwon *et al.* (2021), Yu *et al.* (2015), Simon *et al.* (2009), Rinaldi *et al*.

*Corresponding author, Ph.D.
E-mail: canh.tran1512@gmail.com
[a]Ph.D. Professor
[b]Ph.D. Student
[c]Ph.D.
[d]Ph.D.

ISSN: 2005-307X (Print), 2092-6219 (Online)

(2008), Lim *et al.* (2017), Papanicolaou (2007), Tran *et al.* (2019). In a study by Yu *et al.* (2015), riverbank experiments on non-cohesive and cohesive soils were carried out to examine riverbank erosion due to fluvial hydraulic forces. The experiments revealed that non-cohesive soil experienced failure near the water surface, while cohesive soils were destroyed near the toe of the slope. The study suggested that erosion was directly proportional to flow velocity, and a repeated cycle of slope toe destruction under hydraulic action led to a cantilever phenomenon, reducing shear resistance and causing landslides. Zhou *et al.* (2024) used simulations to show that early-stage bank damage can escalate into more severe failures, especially as floodwaters rise. These increasingly severe collapses are driven by the combined effects of hydrostatic confining forces, pore water pressure, and gravitational forces.

Apart from the influence of river flow, water level variations were found to impact riverbank instability (Duong *et al*. 2014, Duan *et al.* 2018, Liang *et al*. 2015, Ahsan *et al.* 2024). Duong *et al.* (2019) utilized Geostudio software to estimate the stability of the Red River in northern Vietnam, investigating the effects of river water level (RWL) fluctuations on riverbank stability. The study highlighted that surcharge loading (> 50 kPa) significantly weakened riverbanks, becoming the dominant factor controlling the safety factor. Schliewe and de Menezes (2021) conducted experiments to study erosion by waves on the lakeshore of lateritic soils. The erosion rate increased nonlinearly with the accumulated wave power, varying wave frequencies, and distinct beach slope angles. Gu *et al.* (2020) focused on bank slopes in hydro-fluctuation areas of reservoirs or lakes, where severe erosion occurred due to a lack of protection. The study utilized a tank for wave erosion experiments indicating different soil erosion rates corresponding to rising, falling, and fixed water levels.

Nevertheless, the assessment of the impact of waves on riverbanks has been insufficiently explored and lacks a comprehensive evaluation, particularly in dynamic conditions. This study aims to fill this gap by comprehensively assessing the mechanical behavior of riverbanks under the influence of water waves by centrifuge modeling (Takahashi *et al*. 2019, Exton *et al.* 2019). Given the intricate nature of the soil-water interface, research that delves into the interplay of hydraulics and soil mechanics is relatively scarce. This study is designed with two primary objectives: firstly, to evaluate the variations in wave energy (including wavelength, frequency, and amplitude) using the centrifuge technique, and secondly, to assess the erosion rate based on changes in the riverbank induced by wave conditions. The ultimate goal is to establish a good relationship between the erosion rate and riverbank material response under dynamic wave conditions.

2. Methodology

2.1 Centrifuge modeling

Centrifuge modeling is a robust technique widely employed in civil engineering, particularly in geotechnical applications. The centrifuge technique is a calibration and comparison tool for the numerical model and a new hypothesis. Its utilization in geotechnical modeling addresses the challenge of replicating soil stress conditions in a prototype that matches the model. Centrifuge technology enables this achievement by subjecting the model to high acceleration levels exceeding the Earth's gravitational acceleration. Based on these principles, centrifuge models are designed to reproduce geotechnical scenarios through scaling laws (Garnier *et al.* 2007). The versatility of centrifuge technology extends its application to various fields, including geotechnics, hydraulics, structures, and wind tunnels, owing to its convenience and efficiency in constructing small models. This study conducted centrifuge tests at the Geotechnical Centrifuge and Shaking Table Laboratory of the National Central University (Hung *et al.* 2022, Park *et al.* 2021).

Table 1 Test schedule

Group of tests	Test name	Type of soil	Condition
Dynamic pressure test	DW	Without soil	Without riverbank
	DR	Without soil	Rigid riverbank
Erosion Test	ES	Loamy sand	Riverbank
	EML	Silty loam	Riverbank
	EL	Loam	Riverbank
	EC	Clay (without silt)	Riverbank

2.2 Test procedure

In this investigation, the test schedule is outlined in Table 1. The centrifugal experiments were categorized into dynamic pressure tests and erosion tests. The first group comprised two tests, DW (Dynamic _without soil) and DR (Dynamic _ rigid riverbank), conducted without soil to assess wave parameters (wavelength, amplitude, and frequency) and the impact pressure of waves directed toward the rigid riverbank. Furthermore, four experiments were conducted wherein the riverbank was compacted with different types of soil: loamy sand (ES), silty loam (EML), loam (EL), and clay (without silt) (EC) to estimate an erosion rate of the riverbanks.

3. Soil properties and test procedure

3.1 Soil properties

The mixture soil was classified by the USDA agricultural soil classification system in this study. Four samples were employed to replicate riverbank models, each characterized by varying percentages of grain distribution – namely, loamy sand, loam, silty loam, and clay (without silt) in Fig. 1. Particle distribution analysis was conducted to generate the particle distribution curve, as illustrated in Fig. 2. The sand properties included a d_{50} of 0.19 mm, a d_{60}

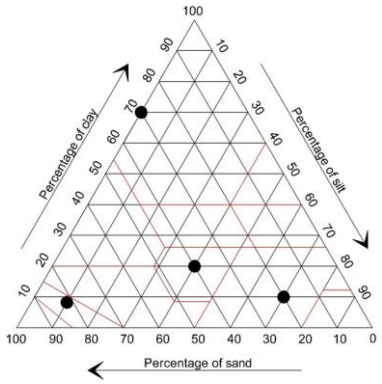

Fig. 1 Soil classification

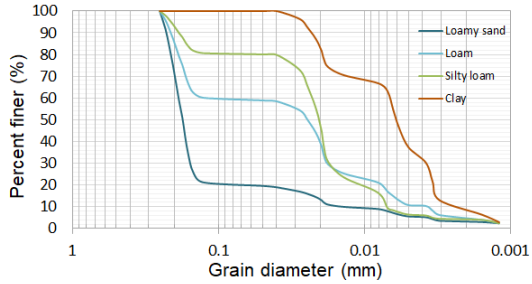

Fig. 2 Grain distribution curve

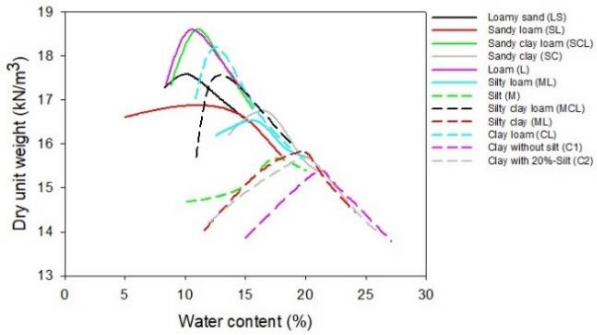

Fig. 3 Compaction test

of 0.2 mm and a d_{10} of 0.15 mm. By examining the relationship between d_{60} and d_{10} along with the grain curve, it was determined that the sand exhibits a uniform particle size.

The specific gravity of sand was 2.65. The dry maximum and minimum unit weights were 16.3 kN/m³ and 14.1 kN/m³, respectively. The frictional angle of the sand was measured at 35 degrees, with a relative density of 40 %. According to the Unified Soil Classification System (USCS), the sand was classified as poorly graded sand (SP) due to its uniform and fine-grained nature. The characteristics of the silt material included a d_{50} of 0.019 mm, a d_{60} of 0.02 mm, and a d_{10} of 0.008 mm. Upon analysing the relationship between d_{60} and d_{10} along with the grain curve, it was determined that the silt exhibits a uniform particle size distribution, categorizing it as poorly graded. According to the Unified Soil Classification System (USCS), this silt was classified as low plasticity silt (ML).

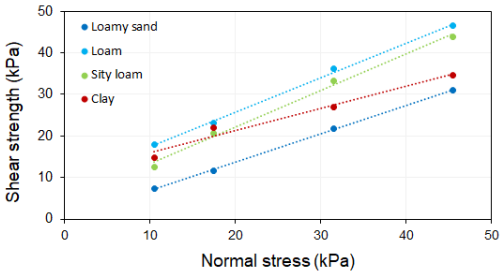

Fig. 4 Direct shear test

The specific gravity of the silt was measured at 2.56. Hydrometer analysis was performed to determine the grain distribution of clay, revealing a d_{50} value of 0.014 mm. According to the Atterberg method, the clay exhibits high plasticity, with a plastic limit of 25, a liquid limit of 58.5, and a plastic index of 33.5. The specific gravity of the clay is measured at 2.45.

The Proctor compaction standard was applied to find the relationship between optimum water content and dry unit weight. The compaction test result is presented in Fig 3. In this research, the author utilized mixing materials with different percentages of component material. The highest dry unit weight was about 18.6 kN/m^3 in loam and sandy clay loam, where grain distribution was not uniform. The lowest dry unit weight was around 15 kN/m^3 in coarse uniform material (sand). In this result, the uniform soil (sand and sandy loam) was challenging to get a peak point of compaction curve. The direct shear test was conducted to obtain the cohesion and friction angle in Fig. 4.

3.2 Test procedure

3.2.1 Water pressure test

In the test "DW", the cylinder was positioned at the end side of the container, and water was added until it reached the desired level. Subsequently, the model was placed on the centrifuge platform, and the centrifuge was then set to speed, getting an artificial acceleration of 20 g. Cameras were strategically placed to capture the wave generation process during the centrifugal test. Within the centrifugal test, the cylinder was connected to an air pump, facilitating the regulation of push and pull cycles. The configuration of the cylinder control system is depicted in Fig. 5. Initially, the air pump was connected to a magnetic valve, which played a crucial role in controlling the opening and closing of airflow to the cylinder. Ultimately, the magnetic valve was linked to the computer, enabling automated control of the entire system through LabVIEW.

In the test "DR", the rigid riverbank was placed opposite side of the cylinder. Upon reaching the artificial acceleration, the cylinder was controlled to generate waves. Pore water pressure transducers were arrayed on the rigid riverbank to measure impact pressure at frequencies ranging from 0.25 Hz to 0.5 Hz, 0.625 Hz, and 1 Hz. A steel plate was utilized to simulate a riverbank with an inclined angle of 60 degrees. Three strategically pore water pressure sensors (P-SWL, P-U1.2, and P-U2.6) were placed along the inclined steel plate,

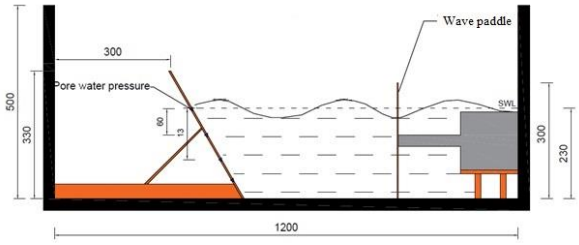

Fig. 5 The configuration of water pressure test

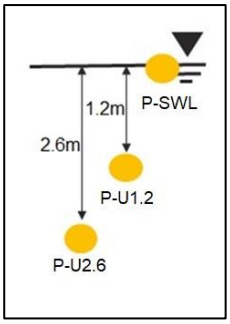

Fig. 6 Water pressure sensor's location

corresponding at the water surfaces and 1.2 m and 2.6 m in water depth, respectively. The water level was adjusted to 23 mm in the model, corresponding to 4.6 m in the prototype.

Waves were generated by controlling the air cylinder on the opposite side. This experimental setup allowed for examining dynamic water pressures along the riverbank under various wave frequencies and conditions.

3.2.2 Erosion test

In the erosion test (ES, EML, EL, EC), the soil was compacted into the container with the slope geometry of 330 mm in height, 300 mm at the top, 490.5 mm at the bottom of a slope, and 300 mm in width (Fig. 5). Plastic sheets were attached to the container edges before compacting the soil to mitigate boundary effects between the container and soil material. The cylinder, connected to a wave-generating paddle, was positioned on the opposite side of the container. Additionally, a wooden plate was set up to provide horizontal support for straightforward soil density regulation. The soil, mixed to the desired percentage and water content determined by compaction tests, was layered into the model in 11 increments, each 30 mm in thickness. Gravel particles were placed on the acrylic side during compaction to measure slope displacement. Three pore water pressure transducers were inserted into the riverbank to monitor changes in pore water pressure in Fig. 6. After compaction, the model was cut to achieve a 60-degree slope, as depicted in Fig. 7. Post-compaction, the total model weight was measured to calculate centrifuge unbalance. The model was then placed on the centrifuge platform. A scanner was employed to scan the model's surface before and after the test, facilitating a comparison of slope changes. A side-view camera captured slope failure during centrifuge spinning. Transducers and sensors were linked to a data logger, transmitting data to the control

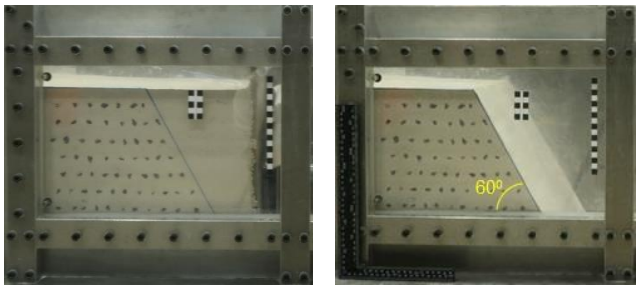

(a) Compaction process (b) A completed model

Fig. 7 Riverbank after compaction

computer. Before centrifuge spinning, water was added to the model, reaching a level of 230 mm. In the post-test, the model was extracted from the centrifuge, and further measurements were taken by cutting it to assess water content and soil strength using the Torvane device.

4. Riverbank behaviors

4.1 Water pressure test

In the test "DW", the model was operated at two frequencies: 0.5 Hz and 1 Hz, corresponding to 0.025 Hz and 0.05 Hz in the prototype, respectively (Fig. 8). The results revealed that the system generated waves with varying characteristics: a wave height of 11.18 mm at 1 Hz and 11.85 mm at 0.5 Hz and a wavelength of 144 mm at 1 Hz and 214.57 mm at 0.5 Hz in the model. The centrifuge modeling outcomes indicated that the wave height at 0.5 Hz (11.18 mm) was less than that at 1 Hz (11.85 mm). Furthermore, the wavelength of 0.5 Hz was 214.57 mm, equivalent to 4.3 m in the prototype, exceeding that of 1 Hz (144 mm, equivalent to 2.88 m in the prototype). Regarding wave height, the wave energy density for the 0.5 Hz and 1 Hz pushing frequencies were approximately 60 J/m² and 70 J/m² in the prototype, respectively. The dynamic pressure (without decay) at the lower frequency of 0.5 Hz (0.025 Hz in the prototype) measured 2.2 kPa in the prototype, lower than the higher frequency of 1 Hz (0.05 Hz in the prototype), which registered around 2.4 kPa in the prototype. Table 2 outlines the wave parameters in both the model and the prototype.

In the test "DR" with the rigid riverbank, this experiment aimed to assess dynamic water pressure variations along the riverbank and the distinctions between static and dynamic pressure conditions. The peak dynamic pressure is consistently measured between 27 and 29 kPa at the water's surface. Nevertheless, the duration of impact varied based on the frequency, a factor that could significantly influence the erosion process. Conversely, the dynamic pressure exhibited a consistent trend at 1.2 m and 2.6 m depths below the water's surface. At a depth of 1.2 m, the maximum affected pressure ranged from 8 to 10 kPa, while at 2.6 m, it ranged from 4 to 6 kPa in Table 3. Fig. 9 illustrates that dynamic pressure decreases with increasing water depth, reaching its maximum at the still water surface. The table below presents the impact pressure at various frequencies, offering a comprehensive overview of wave effects on the riverbank under different conditions.

Table 2 Wave parameters in the model and prototype scale

Wave parameters		Group 1	Group 2
Wave frequency (F_m=NF_p)	Model (Hz)	0.5	1
	Prototype (Hz)	0.025	0.05
Water depth (h_p=Nh_m)	Model (mm)	230	230
	Prototype (m)	4.6	4.6
Wave height (h_p=Nh_m)	Model (mm)	11.18	11.85
	Prototype (m)	0.22	0.24
Wavelength (L_p=NL_m)	Model (mm)	214.57	144
	Prototype (m)	4.3	2.88
Time period (T_p=NT_m)	Model (s)	2	1
	Prototype (s)	40	20

Where N: Centrifugal acceleration

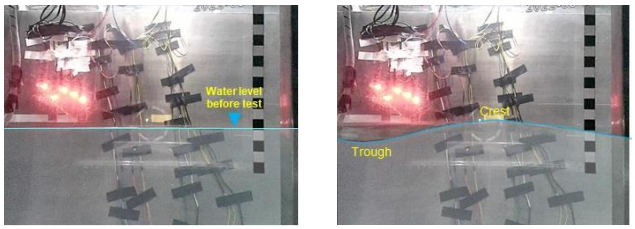

(a) Before test (b) During test

Fig. 8 Wave generation

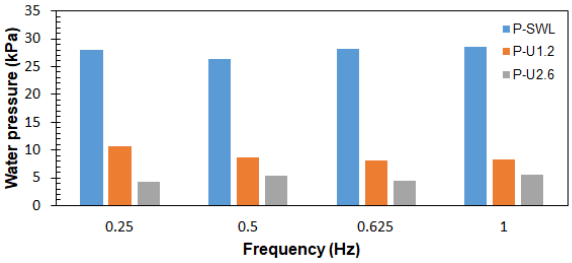

Fig. 9 The distinctions between static and dynamic pressure

Fig. 10 illustrates the distinctions between static and dynamic pressure under dynamic conditions. The disparities were approximately 28 kPa, 9 kPa, and 5 kPa at the still water level, 1.2 m, and 2.6 m beneath the water level, respectively. The difference became more pronounced at the still water surface, reaching three times the values observed at other depths. This escalation was attributed to the dynamic pressure being considerably higher than the static pressure. The dynamic impact pressure decreased with water depth, peaking near the water surface, aligning with results obtained from numerical modeling (Chu *et al.* 2022).

Furthermore, as the water depth increased, the difference diminished because of a slower water flow from the surface to the bed, consistent with findings from previous studies (Zrostlík *et al.* 2015). The results demonstrated that the frequency induced by the wave paddle did not affect the impact pressure of the wave. The amplitude of dynamic pressure was similar at different frequencies at each location.

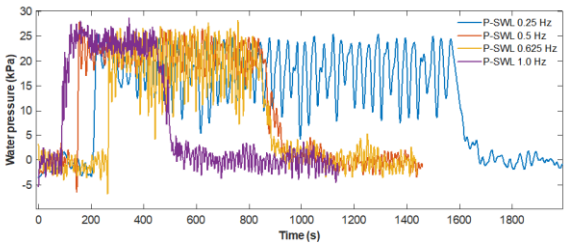

(a) At still water level

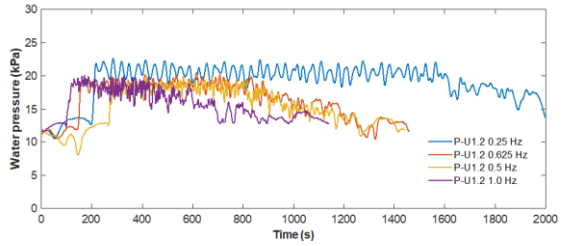

(b) Under water level 1.2 m

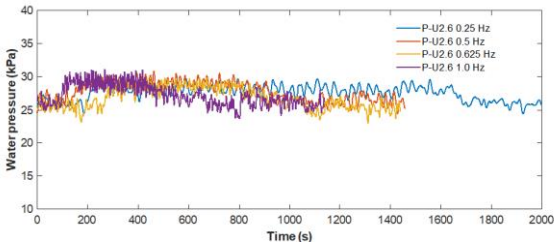

(c) Under water level 2.6 m

Fig. 10 Time history of water pressure

4.2 Erosion test

4.2.1 Centrifuge test results

This section presented the outcomes of erosion tests, including ES, EML, EL, and EC, encompassing details such as process failure, erosion rate, failure shape, and safety factor. In the "EC" experiment involving clay material, 30% sand and 70% clay were used to prepare the model. The results indicated that erosion occurred below the water level, as depicted in Figs. 11(a) and 11(b). The entire test spanned one hour in model scale (20 hours in prototype), and no tension cracks appeared on the surface. Notably, the erosion process did not cause damage to the soil above the water level. The riverbank surface experienced erosion of approximately 0.3 m to 0.6 m (equivalent to 0.045 H to 0.09 H) in the prototype scale, measured from the original surface. A scanner was employed to assess the alteration in the slope surface before and after the test. Post-testing settlement reached 10 mm in the model, equivalent to 0.2 m in the prototype (Figs. 11(c) and 11(d)). The failure surface was identified at the slope's toe, and the erosion distance was indicated by the black dash-line, marking the deepest point of erosion. The collapse of the slope soil amounted to 9.4% (0.47% per hour) in planar strain relative to the slope section.

In this investigation, the erosion process was categorized into three distinct stages: the erosion stage, the tension crack stage, and the failure stage (referred to as Fig. 12). The manifestation of these stages varied depending on

Table 3 Impact pressure under different frequencies

Location	Frequency (Hz)	Maximum pressure (kPa)	Minimum pressure (kPa)	Average pressure (kPa)
At still water level	0.25	28.08	4.18	17.91
	0.50	26.45	15.10	21.55
	0.625	28.24	4.13	19.93
	1.0	28.63	20.19	23.88
Under water level 1.2 m	0.25	22.39	17.75	20.49
	0.50	20.46	16.70	18.80
	0.625	19.96	15.92	18.33
	1.0	20.08	15.37	18.28
Under water level 2.6 m	0.25	29.73	26.00	28.17
	0.50	30.87	27.28	29.13
	0.625	29.88	26.15	28.15
	1.0	31.08	27.14	29.17

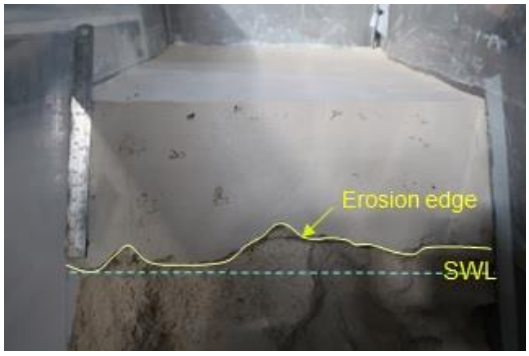

(a) Top view

(b) Front view

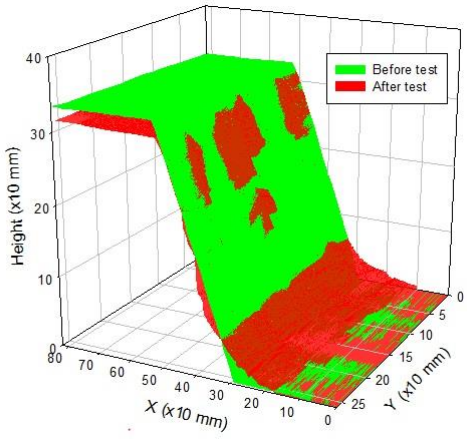

(c) The scanning results in 3D (in model scale)

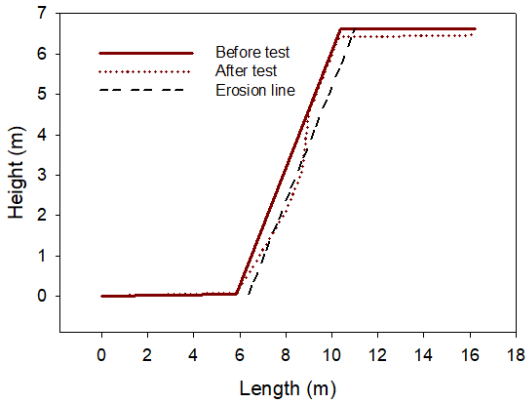

(d) The erosion line after test (in prototype scale)

Fig. 11 The failure of riverbank after test

the type of material and the duration of each stage. During the initial stage, termed the erosion stage, soil from the slope surface was gradually washed away and transported farther down the slope. Remarkably, the slope maintained its stability at this point. Subsequently, the second stage, labeled the "tension crack stage," ensued. In this phase, a more incredible amount of soil was eroded compared to the first stage, resulting in the formation of a cantilever shape and a subsequent decrease in soil-resistant force. Consequently, tension cracks became apparent on the slope surface. Throughout these three stages, the tension crack continued to deepen until the eroded portion eventually collapsed into the water, marking the culmination of the erosion process.

Following the erosion test in Table 4, the clay material (namely, “EC”) exhibited an erosion distance of 0.09H

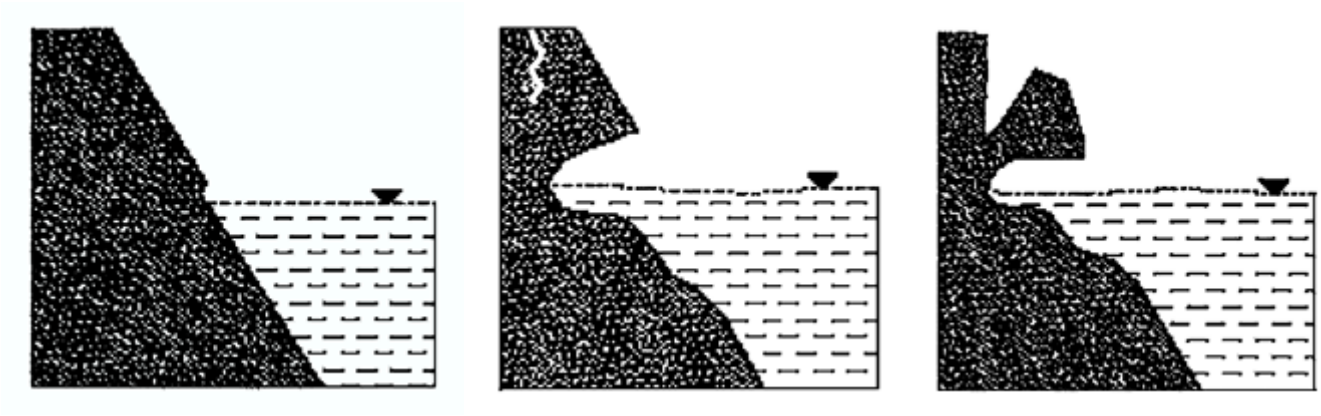

Stage 1: Erosion stage Stage 2: Tension crack stage Stage 3: Failure stage

Fig. 12 Three stages of failure process

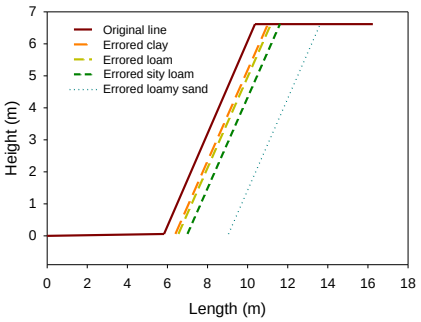

Fig. 13 Eroded line

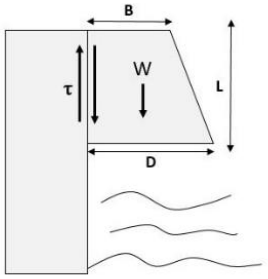

Fig. 14 Failure mechanism of riverbank

(where H represents the slope height), the smallest among all models. In contrast, the loamy sand material (ES) demonstrated the most significant erosion distance at 0.5H. After monitoring time, the test “EC and EL” were stable compared to the others.

Fig. 13 displays the eroded line assumed at the deepest washing point of the surface slope after the test. The results indicated that the soil with a higher percentage of grain content, like "loamy sand, ES" with 80% of sand, was eroded deeper than the soil with a high percentage of fine content (clay and loam). However, the different percentages of sand in "loam" – 40 % and "clay" – 30 % did not significantly affect the erosion distance (D); the ratio was approximately 0.09 H to 0.1 H. However, the "silty loam" with 20% of sand exhibited an erosion distance (0.2 H) larger than the "clay, EC" and "loam, EL" materials. This difference was attributed to the lower percentage of clay (10%) in the "silty loam, EML" compared to "clay" and "loam”.

Consequently, the percentage of grain content significantly affected the erosion process of the riverbank. Under wave conditions (short-term condition), the limitation of material was less than 40 % of sand and higher than 20 % of clay to contribute positively to the slope stability. This suggested that the materials with a higher proportion of sand exhibited a more considerable erosion distance than those with a lower percentage of sand.

Utilizing the erosion distance as a basis, a simple model was developed to establish a relationship between the erosion distance (D) and the percentage of clay, expressed by the following equations. Consequently, a decrease in the percentage of clay corresponded to an increase in the erosion distance. It was worth noting that this relationship exhibited a non-linear nature.

The failure mechanism was illustrated using the limit equilibrium method, as depicted in Fig. 14. This depiction showcased the identification of the failed cantilever under wave conditions. This depiction showcased the identification of the failed cantilever under wave conditions. The safety factor assessment considered the soil's strength and the erosion's geometry. Applying the formula (1) and (2), an increase in material strength or a reduction in the sum of the crown distance (B) and the erosion distance (D) contributed to an enhancement in erosion stability. The factor of safety (F_s) equaling one signified a stable cantilever slope, whereas a factor of safety less than one indicates failure. The critical erosion distance (D_c) was defined when the safety factor was equal to one. It was important to note that these formulas, as described, did not explicitly capture the relationship between wave energy and erosion distance. Further exploration may be necessary to understand better the influence of wave energy on the erosion process.

$$D = 0.482\, x^{-0.38} \quad \text{(With } x\text{: the percent of clay)} \tag{1}$$

$$F_s = \frac{\text{Shear strength}}{\text{Shear stress}} = \frac{S_u}{\tau} \tag{2}$$

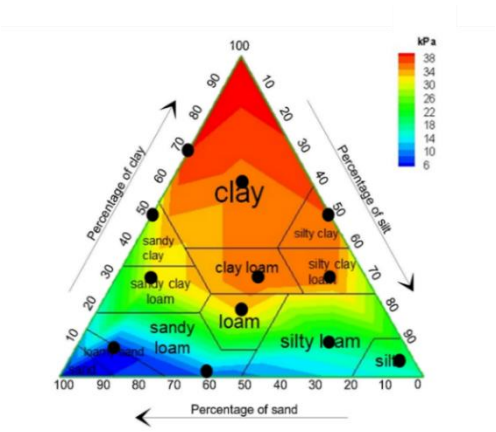

Fig. 15 Soil strength

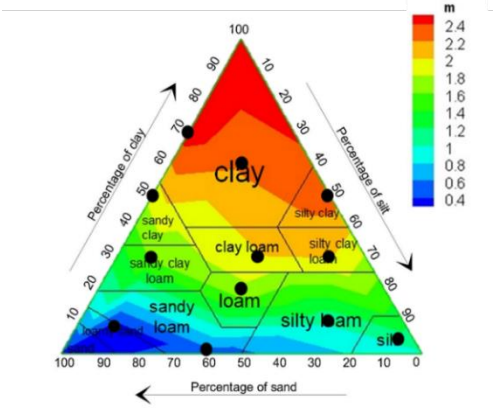

Fig. 16 Critical erosion distance

$$F_s = \frac{2S_u}{\gamma(B+D)} = \frac{2S_u}{\gamma\left(2B + \frac{L}{\tan\alpha}\right)} \quad (3)$$

(α: riverbank angle (°))

Figs. 15 and 16 presents the critical erosion distance determined by considering both soil strength. Notably, the critical erosion distance within the "clay zone" surpassed that of the "loam zone" and "sand zone," exceeding 2 meters. Conversely, the critical erosion distance in the sand zone was less than 1 meter due to the absence of cohesion in this soil type (sand zone, silt zone). Furthermore, within the “silty loam” category, those with lower silt composition exhibited a larger critical erosion distance (1-2 meters) than those with higher silt composition, with less than one meter of critical erosion distances. These distinctions arose from variations in soil composition.

The erosion rate was determined by establishing a correlation between impact pressure and the soil's strength, as illustrated in Fig. 17. Consequently, under a dynamic pressure of 28 kPa and a monitoring duration of 20 hours, the erosion rates for "clay", "loam," and "silty loam" were found to be 0.03 m/h, 0.0375 m/h, and 0.078 m/h, respectively. The relationship between erosion rate and impact pressure exhibited an inverse trend; as the impact pressure increased, the erosion rate decreased.

The presence of multiple variables within wave parameters, including wave height, wavelength, and wave frequency, posed a significant challenge in accurately estimating the erosion rate.

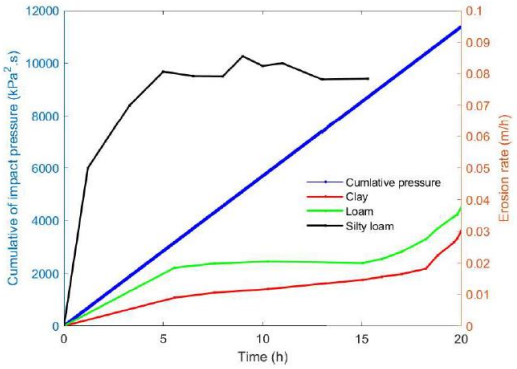

Fig. 17 The relationship between erosion rate and cumulative of impact pressures

The cumulative impact pressure was employed as a simplifying factor in the estimation process to address this complexity. Subsequently, a simplified model was proposed to establish the relationship between the erosion rate and cumulative of wave impact pressure, expressed by the following equation.

$$\varepsilon_t = a \times \left(\frac{\int |P(t)|^2 dt}{S_u}\right)^b \quad (4)$$

Where: P: Cumulative of impact dynamic pressure of water ($kPa^2.s$);
S_u: Untrained shear strength of soil (kPa);
a, b: Empirical coefficient (a=9x10^{-7}, b=1.83);
ε_t: Erosion rate (m/h);

4.2.2 Numerical modeling results

Numerical simulation was employed to assess the safety factor of the model both before and after testing under a stable water level condition. The numerical model simulated changes in slope geometry based on erosion distances observed during testing, with the initial slope depicted as Fig. 18(a) in the prototype scale. In the "EC" test, two materials, encompassing clay and bedrock, were input into the numerical model. Clay simulated the slope material in the centrifugal test, while the bedrock was the container's bed, controlling the slip failure surface that did not extend beyond the slope's toe. Consistent control was applied to the entrance and exit of the slip failure surface across all models, facilitating easy comparison of safety factor variations. In the post-centrifugal test slope geometry represented by Figs. 18(b) and 18(c), with the erosion distance of 0.6, 2.4 m, the safety factor analyzed by the numerical model was 1.319, 0.603, respectively. Notably, the erosion distance was arbitrarily selected to calculate the safety factor.

Consequently, the erosion process has not impacted global failure at present. The assumed erosion distance was introduced to identify the critical erosion. The safety factor increased from 1.311 to 1.319 before and after erosion (0.6 m). However, as the erosion distance extended to 2.0 m, the safety factor decreased to 1.255 and dropped below 1.0 at 2.2 m. Fig. 18(d()presents the safety factor and erosion distance in four types of material. The safety factor was equal to one when the erosion distance was equal to 0.8 m, 1.2 m, and 2.1 m, corresponding to silty loam, loam, and clay material.

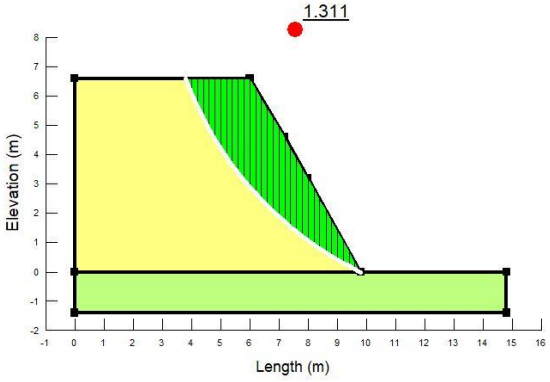

(a) The original slope (EC-model)

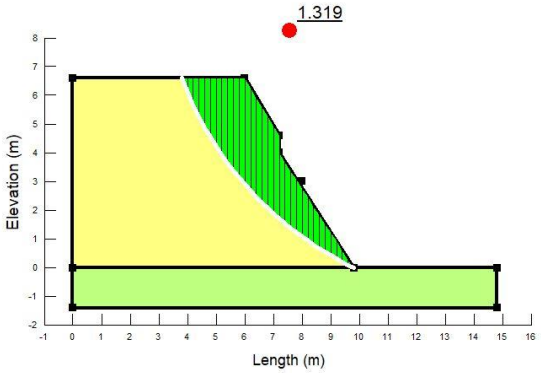

(b) The slope with the erosion depth of 0.6 m (EC-model)

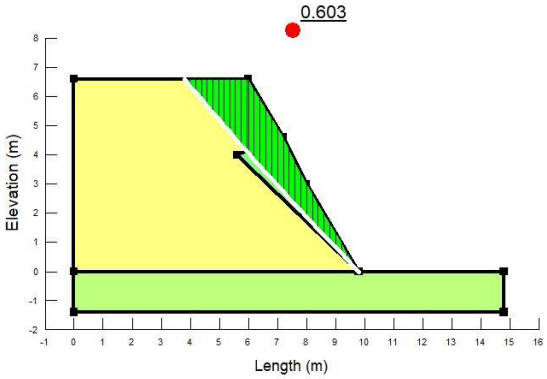

(c) The slope with the erosion depth of 2.4 m (EC-model)

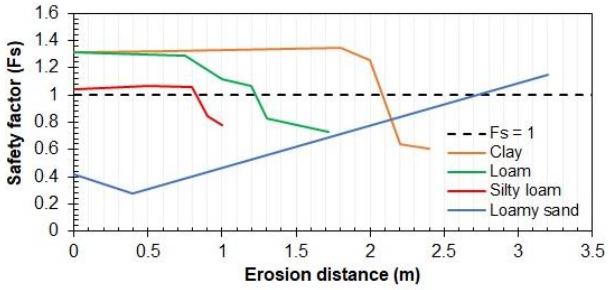

(d) The safety factor during process failure

Fig. 18 The safety factor of slope with different erosion depth

Table 4 Summary of three approaches

Type of soil	Erosion distance (m)		
	Centrifuge results	Theoretical results	Numerical results
Clay	> 0.60 (Still stable)	2.2	2.1
Loam	> 0.75 (Still stable)	1.4 - 1.6	1.2
Silty loam	1.20 (Failed)	1.0 - 1.2	0.8

Table 4 displays the outcomes obtained through three distinct approaches: centrifuge modeling, numerical simulations, and theoretical results. For silt loam material, the erosion distance remained consistent across all three approaches. However, for clay and loam, the centrifuge model tests did not reach the failure stage, resulting in non-equivalent erosion distances compared to numerical simulations and theoretical predictions. The new formula was employed to predict the eroded distance for clay and loam materials. Consequently, the critical erosion distances for clay and loam were determined to be 2.1 m and 1.4 m after 70 hours and 40 hours, respectively. This emphasizes the effectiveness of the centrifuge model in accurately simulating wave conditions, providing valuable insights into erosion dynamics for different soil types.

5. Conclusions

Centrifuge modeling tests were conducted to investigate wave generation under high gravitational conditions and the resulting erosion patterns along riverbanks. The findings provide valuable insights into predicting riverbank erosion under varying wave conditions and with different riverbank materials. This study plays a critical role in evaluating riverbank stability by enhancing our understanding of the interaction between water pressure and soil structure. The results offer essential knowledge of the mechanisms governing riverbank behavior, contributing to the development of effective strategies for erosion control, slope stabilization, and sustainable riverbank management.

The erosion rate was found to depend on factors such as clay content, cumulative impact pressure, and soil strength. Specifically, erosion distance increases with a higher percentage of clay, reaching approximately 2.0 m to 2.4 m. In contrast, the "sand and silt zone" exhibits significantly shorter erosion distances, ranging from 0.4 m to 0.8 m.

The amplitude of dynamic pressure varies significantly at the water surface, while the difference between static and dynamic pressures decreases nonlinearly with increasing water depth. Under conditions of constant wave height, the impact pressure remains similar, indicating that wave frequency does not influence instantaneous impact pressure.

However, wave frequency is a crucial factor in determining the cumulative impact pressure over time. For future research, the influence of time-dependent factors on riverbank stability should be further investigated to achieve a more comprehensive understanding of riverbank behavior under prolonged wave action.

Acknowledgments

The authors gratefully acknowledge the support provided by the Geotechnical Centrifuge and Shaking Table Laboratory at National Central University in Taoyuan, Taiwan and National Center for Research on Earthquake Engineering (NCREE) in Taipei, Taiwan, for their valuable contributions and insightful discussions throughout the research process.

References

Ahsan, M.T., Wang, J.P. and Dadda, A. (2024), "Numerical analysis of riverbank slope stability considering rainfall, vegetation and water level fluctuation", *J. Eng. Res Sci*., **3**(4), 20-31. https://doi.org/10.55708/js0304003.

Ayadat, T. and Hanna, A. (2008), "Effects of hydraulic shear stress and rate of erosion on the magnitude, degree, and rate of collapse", *Geomech. Geoeng*., **3**(1), 59-69. https://doi.org/10.1080/17486020701759644.

Beltaos, S., Carter, T., Rowsell, R. and DePalma, S.G. (2018), "Erosion potential of dynamic ice breakup in Lower Athabasca River", Part I: Field measurements and initial quantification", *Cold Reg. Sci. Technol.*, **149**, 16-28. https://doi.org/10.1016/j.coldregions.2018.01.013.

Billah, M.M., Majumdar, A., Rahman, S.M.A., Alam, M.S., Hossain, M.J., Talukder, J. and Khanam, T. (2023), "Riverbank erosion and rural food security in Bangladesh", *World*, **4**(3), 528-544. https://doi.org/10.3390/world4030033.

Van, C.T., Son, N.T. and Tuan, N.C. (2021), "Research and experimental application of empirical formulas to calculate riverbank erosion in Tien River in the Mekong Delta", *J. Environ. Sci. Eng.*, **10**, 116-123. https://10.17265/2162-5298/2021.03.003.

Chassiot, L., Lajeunesse, P. and Bernier, J.F. (2020), "Riverbank erosion in cold environments: Review and outlook", *Earth-Sci. Rev.*, **207**, 103231. https://doi.org/10.1016/j.earscirev.2020.103231.

Choi, C.E., Cui, Y., Au, K.Y.K., Liu, H., Wang, J., Liu, D. and Wang, H. (2018), "Case study: effects of a partial-debris dam on riverbank erosion in the Parlung Tsangpo River, China", *Water*, **10**(3), 250. https://doi.org/10.3390/w10030250.

Chu, C.R., Huynh, L.E. and Wu, T.R. (2022), "Large eddy simulation of the wave loads on submerged rectangular decks", *Appl. Ocean Res.*, **120**, 103051. https://doi.org/10.1016/j.apor.2022.103051.

Duan, G., Shu, A., Rubinato, M., Wang, S. and Zhu, F. (2018), "Collapsing mechanisms of the typical cohesive riverbank along the Ningxia–inner Mongolia catchment", *Water*, **10**(9), 1272. https://doi.org/10.3390/w10091272.

Duong Thi, T. and Do Minh, D. (2019), "Riverbank stability assessment under river water level changes and hydraulic erosion", *Water*, **11**(12), 2598. https://doi.org/10.3390/w11122598.

Duong, T.T., Komine, H., Do, M.D. and Murakami, S. (2014), "Riverbank stability assessment under flooding conditions in the Red River of Hanoi, Vietnam", *Comput. Geotech.*, **61**, 178-189. https://doi.org/10.1016/j.compgeo.2014.05.016.

Exton, M., Harry, S., Kutter, B., Mason, H.B. and Yeh, H. (2019), "Simulating tsunami inundation and soil response in a large centrifuge", *Scientific Reports*, **9**(1), 11138. https://doi.org/10.1038/s41598-019-47512-x.

Garnier, J., Gaudin, C., Springman, S.M. Culligan, P.J., Goodings, D., Konig, D. and Thorel, L. (2007), "Catalogue of scaling laws and similitude questions in geotechnical centrifuge modelling", *Int. J. Phys. Modell. Geotech.*, **7**(3), 01-23. https://doi.org/10.1680/ijpmg.2007.070301.

Gu, J., Liu, G., Abd Elbasit, M.A.M. and Shi, H.Q. (2020), "Response of slope surface roughness to wave-induced erosion during water level fluctuating", *J. Mountain Sci.*, **17**(4), 871-883. https://doi.org/10.1007/s11629-019-5745-8.

Hung, W.Y., Tran, M.C. and Bui, V.K. (2022), "Seismic response of anchored sheet pile walls by centrifuge modelling tests", *Int. J. Civil Eng.*, **20**(9), 1041-1065. https://doi.org/10.1007/s40999-022-00710-7.

Jia, D., Shao, X., Wang, H. and Zhou, G. (2010), "Three-dimensional modeling of bank erosion and morphological changes in the Shishou bend of the middle Yangtze River", *Adv. Water Resour.*, **33**(3), 348-360. https://doi.org/10.1016/j.advwatres.2010.01.002.

Kwon, Y.M., Cho, G.C., Chung, M.K. and Chang, I. (2021), "Surface erosion behavior of biopolymer-treated river sand", *Geomech. Eng*., **25**(1) 49-58. https://doi.org/10.12989/gae.2021.25.1.049.

Lim, K., Li, A.J., Schmid, A. and Lyamin, A.V. (2017), "Slope-stability assessments using finite-element limit-analysis methods", *Int. J. Geomech.*, **17**(2), 06016017. https://doi.org/10.1061/(ASCE)GM.1943-5622.0000715.

Liang, C., Jaksa, M.B., Ostendorf, B. and Kuo, Y.L. (2015), "Influence of river level fluctuations and climate on riverbank stability", *Comput. Geotech.*, **63**, 83-98. https://doi.org/10.1016/j.compgeo.2014.08.012.

Nguyen, S.H., Huynh, T.T., Bui, V.T. and Van Dau, N. (2021), "The mechanism of riverbank erosion caused by ship-generated waves along Hau river's entrance navigation channel, Southern Vietnam", *Adv. Sustain. Constr. Resour. Management*, 897-904. https://doi.org/10.1007/978-981-16-0077-7_73.

Mondal, M.S.H., Murayama, T. and Nishikizawa, S. (2021), "Examining the determinants of flood risk mitigation measures at the household level in Bangladesh", *Int. J. Disaster Risk Reduct.*, **64**, 102492. https://doi.org/10.1016/j.ijdrr.2021.102492.

Oberhagemann, K. and Hossain, M.M. (2011), "Geotextile bag revetments for large rivers in Bangladesh", *Geotext. Geomembranes*, **29**(4), 402-414. https://doi.org/10.1016/j.geotexmem.2010.12.003.

Park, S., Kim, J.H., Kim, S.J., Park, J.H., Kwak, K.S. and Kim, D.S. (2021), "Centrifuge modelling of rock-socketed drilled shafts under uplift load", *Geomech. Eng.*, **24**(5), 431-441. https://doi.org/10.12989/gae.2020.23.4.365.

Papanicolaou, A.N., Elhakeem, M. and Hilldale, R. (2007), "Secondary current effects on cohesive river bank erosion", *Water Resour. Res.*, **43**(12). https://doi.org/10.1029/2006WR005763.

Paul, B.K., Rahman, M.K., Crawford, T., Curtis, S., Miah, M.G., Islam, M.R. and Islam, M.S. (2020), "Explaining mobility using the community capital framework and place attachment concepts: A case study of riverbank erosion in the lower Meghna Estuary, Bangladesh", *Appl. Geography*, **125**, 102199. https://doi.org/10.1016/j.apgeog.2020.102199.

Prowse, T.D. and Culp, J.M. (2003), "Ice breakup: A neglected factor in river ecology", *Can. J. Civil Eng.*, **30**(1), 128-144. https://doi.org/10.1139/l02-040.

Rinaldi, M., Mengoni, B., Luppi, L., Darby, S.E. and Mosselman, E. (2008), "Numerical simulation of hydrodynamics and bank erosion in a river bend", *Water Resour. Res.*, **44**(9). https://doi.org/10.1029/2008WR007008.

Schliewe, M.S., de Menezes, A.V., Marques, T.A., dos Anjos Mascarenha, M.M., Vasco, J.R.G., da Luz, M.P. and Sales, M.M. (2021), "Experimental study of erosion by waves on the lakeshore of lateritic soils", *J. Hydrol.*, **603**, 127004. https://doi.org/10.1016/j.jhydrol.2021.127004.

Simon, A., Pollen-Bankhead, N., Mahacek, V. and Langendoen, E. (2009), "Quantifying reductions of mass-failure frequency and sediment loadings from streambanks using toe protection and other means: Lake Tahoe, United States 1", *JAWRA J. Am. Water Resour. Association*, **45**(1), 170-186. https://doi.org/10.1111/j.1752-1688.2008.00268.x.

Takahashi, H., Morikawa, Y. and Kashima, H. (2019), "Centrifuge modelling of breaking waves and seashore ground", *Int. J. Phys. Modell. Geotech.*, **19**(3), 115-127. https://doi.org/10.1680/jphmg.17.00037.

Tran, A.T.P., Chang, I. and Cho, G.C. (2019), "Soil water retention and vegetation survivability improvement using microbial biopolymers in drylands", *Geomech. Eng.*, **17**(5), 475-483. https://doi.org/10.12989/gae.2019.17.5.475.

Vandermause, R., Harvey, M., Zevenbergen, L. and Ettema, R. (2021), "River-ice effects on bank erosion along the middle segment of the Susitna river, Alaska", *Cold Reg. Sci. Technol.*, **185**, 103239. https://doi.org/10.1016/j.coldregions.2021.103239.

Yan, G., Cheng, H., Jiang, Z., Teng, L., Tang, M., Shi, T. and Zhou, Q. (2022), "Recognition of fluvial bank erosion along the main stream of the Yangtze River", *Engineering*, **19**, 50-61. https://doi.org/10.1016/j.eng.2021.03.027.

Yu, M.H., Wei, H.Y. and Wu, S.B. (2015), "Experimental study on the bank erosion and interaction with near-bank bed evolution due to fluvial hydraulic force", *Int. J. Sediment Res.*, **30**(1), 81-89. https://doi.org/10.1016/S1001-6279(15)60009-9.

Zhou, Y., Xia, J., Deng, S. and Han, Z. (2024), Bank erosion under the impacts of hydraulic erosion, river stage change and revetment protection in the Middle Yangtze River", *Geomorphology*, **448**, 109043. https://doi.org/10.1016/j.geomorph.2023.109043.

Zheng, S., Xu, Y.J., Cheng, H., Wang, B., Xu, W. and Wu, S. (2018), "Riverbed erosion of the final 565 kilometers of the Yangtze River (Changjiang) following construction of the Three Gorges Dam", *Scientific Reports*, **8**(1), 11917. https://doi.org/10.1038/s41598-018-30441-6.

Zrostlík, Š., Bareš, V., Krupička, J., Picek, T. and Matoušek, V. (2015), "One-dimensional velocity profiles in open-channel flow with intense transport of coarse sediment", *In EPJ Web of Conferences*, **92**, 02120. https://doi.org/10.1051/epjconf/20159202120.